Dihydroceramide desaturase directs the switch between exosome production and autophagy for neuronal maintenance

Authors:

Chen-Yi Wu[1,3,*], Jhih-Gang Jhang[1,*], Chih-Wei Lin[1], Han-Chen Ho[2], Chih-Chiang Chan[1,§], Shu-Yi Huang[3,§]

Affiliations:

1 Graduate Institute of Physiology, College of Medicine, National Taiwan University, Taipei, Taiwan

2 Department of Anatomy, Tzu Chi University, Hualien, Taiwan

3 Department of Medical Research, National Taiwan University Hospital, Taipei, Taiwan

[*] These authors contributed equally to this work.

[§] Corresponding authors:

S.-Y. Huang

ORCID: 0000-0002-3522-0500

E-mail: shuyih@ntuh.gov.tw

Mailing address: No. 7, Zhongshan S. Rd., Zhongzheng Dist., Taipei City 100225, Taiwan

C.-C. Chan

ORCID: 0000-0003-2626-3805

E-mail: chancc1@ntu.edu.tw

Mailing address: No. 1, Sec. 1, Ren'ai Rd., Zhongzheng Dist., Taipei City 100233, Taiwan

Keywords: dihydroceramide desaturase, dihydroceramide, neuron, exosome, autophagy, multivesicular endosome

ABSTRACT

Exosomes play important roles in the nervous system. Mutations in the human dihydroceramide desaturase gene, *DEGS1*, are recently linked to severe neurological disorders, but the cause remains unknown. Here, we show that Ifc is required for the morphology and function of *Drosophila* photoreceptor neurons and not in the surrounding glia, but the degeneration of *ifc-KO* eyes can be rescued by glial expression of *ifc*, possibly mediated by exosomes. We develop an *in vivo* assay using Drosophila eye imaginal discs and show that the level and activity of Ifc correlates with the detection of exosome-like vesicles. While *ifc* overexpression and autophagy inhibition both enhances exosome production, combining the two had no additive effect. Moreover, *ifc-KO* reduces the density of the exosome precursor intraluminal vesicles (ILVs) in vivo, and DEGS1 promotes ILV formation *in vitro*. In conclusion, dihydroceramide desaturase promotes exosome formation and prevents its autophagic degradation in the nervous system.

Introduction

Exosomes are secreted vesicles of approximately 100 nm in diameter that mediate the transport of proteins, RNAs, or lipid cargos. In the central nervous system, exosomes serve as a form of intercellular communication and participate in neurodevelopment, synaptic function, and neuronal maintenance (Budnik et al., 2016). In neurodegenerative diseases, including Alzheimer's disease and Parkinson's disease, exosomes affect disease progression by facilitating the clearance of protein aggregates or the spread of toxic signals (Budnik et al., 2016). Exosomes originate from the invagination of the endosomal membrane in multivesicular endosomes (MVEs) to form intra-luminal vesicles (ILVs) (Raposo and Stoorvogel, 2013). ILVs are formed by a mechanism involving the Endosomal Sorting Complexes Required for Transport (ESCRT) complex of more than 20 proteins that recruit ubiquitinated protein cargos (Katzmann et al., 2001) and facilitate the budding and scission of the membrane to form ILVs into the MVE lumen (Adell et al., 2014). Alternatively, ILVs can also form via an ESCRT-independent, ceramide (Cer)-dependent mechanism. Trajkovic et al. (2008) show that the inhibition of neutral sphingomyelinase blocks the conversion of sphingomyelin to Cer and reduces exosome release from oligodendrocytes, likely because low Cer disfavors membrane budding. Once formed, ILVs inside MVEs may be targeted for autophagic or lysosomal degradation, or be released to the extracellular space as exosomes when the MVE membrane fuses with the plasma membrane. Although a ubiquitin-like post-translational modification called ISGylation has been described to promote MVE degradation and thus block exosome secretion (Villarroya-Beltri et al., 2016), the control of the switch between secretion and degradation remains largely unknown.

37

38 Sphingolipids such as sphingomyelin and Cer are major components of cellular
39 membranes in eukaryotic cells, typically represent ~10-20% of cellular lipids (van Meer
40 et al., 2008). In addition to sphingomyelin hydrolysis, as much as one-third of cellular
41 Cer is produced via the *de novo* synthesis pathway (Lee et al., 2012). The final step of
42 Cer *de novo* synthesis is catalyzed by the enzyme dihydroceramide desaturase (DEGS1 in
43 human and Ifc in *Drosophila*) which inserts a 4,5-*trans*-double bond into the sphingolipid
44 backbone of dihydroceramide (dhCer) to produce Cer. This structural difference has a
45 profound effect on the biophysical properties of Cer; therefore, the relative abundance of
46 Cer versus dhCer in cellular membranes may have a profound impact on microdomain
47 segregation, signal transduction, membrane permeability, and membrane bending
48 curvature (Li et al., 2002). Indeed, genetic or drug inhibition of DEGS1/Ifc has been
49 shown to cause significant accumulation of dhCer which increases reactive oxygen
50 species, induces autophagy and ER stress, causes cell cycle arrest, and even results in cell
51 death (Barbarroja et al., 2015, Flores et al., 1998, Kraveka et al., 2007, Munoz-Guardiola
52 et al., 2020, Siddique et al., 2013). Although ceramide is known to promote exosome
53 biogenesis, the role of dhCer in exosome has never been explored beyond reports of its
54 detection in exosomes (Brzozowski et al., 2018, Podbielska et al., 2016, Vallabhaneni et
55 al., 2015). Considering that autophagy is involved in the degradation of MVE and
56 DEGS1/Ifc inhibition is a potent inducer of autophagy both *in vitro* and *in vivo*
57 (Gagliostro et al., 2012, Hernandez-Tiedra et al., 2016, Jung et al., 2017, Siddique et al.,
58 2013), it is possible that dhCer metabolism may affect the autophagic degradation of
59 MVEs to regulate exosome production and release.

60

61 Three recent reports linked variants of the human dhCer desaturase gene, *DEGS1*,
62 to leukodystrophy and systemic neuropathy (Dolgin et al., 2019, Karsai et al., 2019, Pant
63 et al., 2019). These reports not only confirm an essential role for *DEGS1*in the human
64 nervous system, but they also showed that loss-of-function mutations of *DEGS1*cause
65 significant accumulation of dhCer and a shift of cellular sphingolipid pool towards the
66 dihydro forms. However, the underlying cause of neuropathy remains unknown. Our
67 previous study shows that systemic knock-out of *Drosophila ifc* results in larval lethality,
68 which can be partially rescued tissue-specific expression of *ifc* only in neurons or muscle,
69 suggesting that Ifc can function cell non-autonomously (Jung et al., 2017). We also show
70 that, unlike the conventional belief that the conversion of dhCer to Cer occurs in the ER,
71 Ifc predominantly localizes to the endosomes in *Drosophila* photoreceptors. Furthermore,
72 Ifc colocalizes with an endosomal protein Rab4, which is also known to be enriched in
73 exosomes (Vidal and Stahl, 1993). Therefore, we hypothesized that *ifc* influences
74 exosome biogenesis to exert its cell non-autonomous function. In the present study, we
75 explored the necessity and sufficiency of *ifc* in neurons versus glia for the maintenance of
76 photoreceptor function in the *Drosophila*. We also developed an assay to observe whether
77 *ifc* plays a role in exosome biogenesis *in vivo* using *Drosophila* eye imaginal discs and
78 evaluated the effect of *ifc* inhibition on autophagy versus exosome release. Lastly, we
79 employed the giant unilamellar vesicle (GUV) system to examine the ability of human
80 DEGS1 to promote the formation of ILVs *in vitro*. Our findings demonstrate an important
81 role for DEGS1/Ifc in regulating the switch between autophagy and exosome biogenesis,
82 providing a possible mechanism of its cell non-autonomous function in the nervous

system.

Results

Drosophila ifc is differentially required in photoreceptor neurons versus glia

We have previously reported that *ifc-KO* whole eye clones in *Drosophila* show light-dependent degeneration of photoreceptors as evidenced by the disorganized ommatidial pattern and the decreased depolarizing amplitudes measured by electroretinogram (ERG) (Jung et al., 2017). However, the whole-eye *ifc-KO* clones take out *ifc* in both photoreceptor neurons and the surrounding glia. To further decipher whether *ifc* is required in neurons, glia, or both, we created cell-type-specific *ifc* knock-out clones using two different FLP/FRT site-directed recombination systems. We flanked the *ifc* coding sequence with FRT sites and depleted *ifc* either strictly in the photoreceptor cells using the *ey3.5-FLP* (Mehta et al., 2005) or in the neighboring glial cells by *repo-FLP* (Xiong and Montell, 1995). We found that clonal depletion of *ifc* only in the photoreceptor neurons was sufficient to cause significant neurodegeneration after 10 days of light exposure as evidenced by both the morphological degradation of ommatidial organization (Figure 1A,B, quantified in Figure 1C) and the functional declined in depolarization amplitude measured by ERG (Figure 1D, quantified in Figure 1,E). In contrast, knocking-out *ifc* in the neighboring glial cells caused no significant difference in the morphology of photoreceptors (Figure 1F-H) and only resulted in a slight reduction in the depolarizing amplitudes as detected by ERG (Figure 1I,J). These results indicate that the photoreceptor neurons had a strict requirement for *ifc*, whereas the function of *ifc* in glial cells was

106 likely to be less essential.

107

108 Glial expression of *ifc* rescues the requirement for *ifc* in neurons

109 Our previous report finds that *ifc* expressed in different tissues under different Gal4
110 drivers can rescue the larval lethality phenotype of ubiquitous *ifc-KO*, suggesting cell
111 non-autonomous rescue. Here, we further tested if *ifc* expression in glial cells alone was
112 sufficient to rescue the degenerative phenotype of *ifc-KO* whole-eye clones by comparing
113 the effect of expressing the UAS transgene of wild-type *ifc(WT)-mCherry* in glial cells
114 only (*repo-GAL4*) versus in the whole eye (*GMR-GAL4*). We found that overexpression
115 of *GMR>ifc(WT)-mCherry* and *repo>ifc(WT)-mCherry* both significantly rescued the *ifc-*
116 *KO* whole-eye clones, and the rescue effect was at comparable levels as determined by
117 ommatidial morphology (Figure 2A-E) and functional electroretinogram (Figure 2F,G).
118 Because *ifc* is required in the photoreceptor neurons, the results here show that cell non-
119 autonomous supply of *ifc* from glia to photoreceptor neurons is sufficient to rescue the
120 eye degenerative phenotype of *ifc-KO*.

121

122 Knocking-out *ifc* reduces the density of ILVs in the MVEs

123 One possible mechanism underlying the cell non-autonomous rescue is via exosome, we
124 thus examined the morphology of MVE, the first cellular structure related to exosome
125 production, by analyzing the ultrastructural images of wild-type (WT) and *ifc-KO*
126 photoreceptors by transmission electron microscopy. The MVEs in the WT
127 photoreceptors typically contained densely packed ILVs (Figure 3A). In comparison, the
128 MVEs in the *ifc-KO* photoreceptors appeared bloated (Figure 3B). Indeed, while the

129 numbers of MVE per view field were similar between WT and mutant photoreceptors
130 (Figure 3C, $p = 0.3213$), the size of the MVEs was significantly larger in *ifc-KO*
131 photoreceptors (Figure 3D, $p = 0.0226$). Moreover, the average number of ILVs in each
132 MVE was slightly reduced in *ifc-KO*, although the difference from WT was not
133 statistically significant (Figure 3E, $p = 0.1153$). However, when the size of MVEs was
134 taken into consideration, we found that the density of ILVs was significantly reduced in
135 the mutant MVEs comparing with that of WT (Figure 3F, $p < 0.0001$). This phenotype
136 was reminiscent of some ESCRT complex mutants (Adell et al., 2014, Buono et al., 2017,
137 Teis et al., 2010), suggesting that Ifc may function in the MVEs and participate in the
138 production of ILVs.
139
140 <u>Ifc activity positively correlates with the production of exosome-like vesicles</u>
141 *Drosophila* imaginal discs are capable of secreting exosomes (Gross et al., 2012). We
142 collected particles released by *Drosophila* eye imaginal discs and determined their sizes
143 by nanoparticle tracking analysis. The average diameter of the secreted vesicles was
144 113.8 ± 14.3 nm (Figure S1), consistent with the size range of exosomes. To evaluate the
145 role of *ifc* in exosome biogenesis, we established an *in vivo* system with the eye imaginal
146 discs utilizing the Dorsal-Eye Gal4 (*DE-GAL4*) system (Morrison and Halder, 2010) to
147 express the exosome marker of CD63 fused to GFP (Panakova et al., 2005). In this setup,
148 the expression of UAS-GFP-*CD63* is restricted to the dorsal half of the disc, and the
149 release of GFP-CD63+ extracellular vesicles can be observed on the ventral side,
150 especially in the acellular space above the morphogenetic furrow as evidenced by the
151 absence of DAPI staining (illustrated in Figure 4A). We quantified the GFP-CD63+

152 vesicles in the ventral morphogenetic furrow. In the *ifc-KO* eye disc clones, the number
153 of GFP puncta detected away from the dorsal compartment was significantly reduced in
154 comparison with the control eye discs (Figure 4B-D), suggesting that *ifc* promotes the
155 production of CD63+ extracellular vesicles. We tested another exosome marker, the
156 flotillin protein Flo2-RFP (Bischoff et al., 2013) to further characterize the extracellular
157 vesicles in eye discs. Consistent with the results observed with GFP-CD63, *ifc-KO*
158 reduced the number of Flo2-RFP puncta in the ventral compartment (Figure 4E-G). Since
159 Cer has been shown to promote exosome formation by favoring membrane budding, our
160 data suggest that *ifc-KO* hinders exosome production by affecting membrane properties
161 due to the accumulation of dhCer over Cer.
162
163 Conversely, using another exosome marker TSG101 (Thery et al., 2001), we
164 found that overexpression of *ifc(WT)-mCherry* increased the detection of extracellular
165 puncta labeled with TSG101-HA (Figure 5A-C). We further showed that *ifc* may have a
166 dose-dependent effect on the number of vesicles detected since overexpression of
167 *ifc(WT)-mCherry* increased the number of GFP-CD63+ puncta comparing with the
168 *mCherry-CAAX* as a UAS control (Figure 5D,E,G). To investigate whether the catalytic
169 activity of Ifc was required, we mutated one of the highly conserved histidine boxes that
170 are required for the enzyme activity of Ifc (Figure S2A) (Ternes et al., 2002). Expression
171 of *ifc(C3^{mut})-mCherry* failed to rescue the degeneration phenotype of *ifc-KO* eye clones
172 (Figure S2B-G). The lack of rescue was not due to a difference in the protein level as our
173 Western blot analysis showed that the level of Ifc(C3^{mut})-mCherry was similar to that of
174 Ifc(WT)-mCherry (Figure S2H,I), suggesting a functional deficiency. Consistently,

175 overexpression of *ifc(C3^{mut})-mCherry* did not increase the number of GFP-CD63+ puncta
176 released in comparison with the *mCherry-CAAX* control (Figure 5D,F,G), suggesting that
177 the desaturase activity of Ifc is required to promote the production of GFP-CD63+
178 exosome-like vesicles (ELVs). Together, these findings show that these extracellular
179 vesicles exhibit several main characteristics of exosomes based on exosome marker
180 proteins and the size distribution (Thery et al., 2018), thus support the use of GFP-CD63
181 as a surrogate to monitor the extracellular ELVs produced in the system of *Drosophila*
182 eye imaginal discs. Also, the results demonstrated a correlation between the level and
183 activity of Ifc with the number of ELVs detected.
184
185 <u>Ifc directs the switch between the release of ELVs and their degradation via autophagy</u>
186 We and others have reported autophagy induction as a common outcome of
187 *DEGS1/ifc* inhibition not only in *Drosophila* but also in mammalian cell lines and animal
188 models (Barbarroja et al., 2015, Holland et al., 2007, Jung et al., 2017, Kraveka et al.,
189 2007). Autophagy and exosome pathways are known to be interconnected: inhibition of
190 autophagy has been shown to increase exosome release (Poehler et al., 2014), whereas
191 autophagy induction shifts the fate of ILV-containing MVE for autophagy-mediated
192 degradation thus reduces exosome release (Fader et al., 2008). We examined the
193 localization of CD63 to MVEs and autophagosomes in *Drosophila* eye imaginal discs. In
194 the wild-type controls, very little CD63 colocalized with the autophagosomal marker
195 Atg8a. The colocalization of CD63 and Atg8 dramatically increased in *ifc-KO* eye
196 imaginal discs with a concomitant induction in autophagy indicated by increased Atg8a
197 (Figure 6A-C). On the contrary, the colocalization between CD63 and the MVE marker

198 Rab5 was significantly reduced upon *ifc-KO* (Figure 6D-F). We further examined the
199 colocalization between CD63 and the constitutively active form of Rab5 ($Rab5^{CA}$) in
200 adult eyes. $Rab5^{CA}$ is known to block endosome maturation and has been widely used for
201 analyzing MVE formation (Stenmark et al., 1994, Wegner et al., 2010). Consistently, the
202 level of colocalization between GFP-CD63 and Rab5 also significantly decreased in the
203 enlarged endosomal vesicles in the photoreceptor neurons (Figure S3). The results
204 support that Ifc controls the fate of MVE likely by controlling the targeting of MVEs for
205 autophagy-mediated degradation.
206
207 To further determine the interaction between *ifc* and autophagy, we inhibited
208 autophagy by feeding the *Drosophila* larvae with 3-methyladenine (3-MA) and
209 chloroquine that block the formation of autophagosome and prevent autophagosomes-
210 lysosome fusion, respectively (Tang et al., 2017, Jung et al., 2017). Inhibition of
211 autophagy by 3-MA and chloroquine both increased the numbers of GFP-CD63+ vesicles
212 released in the wild-type background (Figure 7A-D). Consistent with the results shown in
213 Figure 5, over-expression of *ifc(WT)-mCherry* increased the number of ELVs.
214 Interestingly, feeding 3-MA or chloroquine to larvae overexpressing *ifc* did not further
215 increase the number of GFP-CD63 puncta detected in the ventral morphogenetic furrow
216 (Figure 7E-H, compared with 7D). These data suggest that Ifc promotes the production of
217 ELVs by inhibiting autophagy.
218
219 <u>Ifc participates in the early stage of ILV formation</u>
220 Considering the effect of Cer on membrane budding, we hypothesize that Ifc functions in

221 the early step of membrane invagination during ILV formation. Since the role of ESCRT
222 proteins in regulating the process of ILV formation is well studied, we investigated the
223 genetic interactions between *ifc* and the ESCRT-0 gene *hrs* and the ESCRT-II gene *vps-*
224 *25*. Because homozygous mutations of hrs^{D28} and $vps25^{A3}$ are both lethal (Lloyd et al.,
225 2002, Vaccari and Bilder, 2005), we analyzed whether the heterozygous mutation affects
226 exosome production in the eye discs with overexpressing *ifc*. In eye imaginal discs where
227 we overexpressed *ifc(WT)-mCherry* using the *DE-GAL4* system, we found that $hrs^{D28/+}$
228 greatly reduced the number of GFP-CD63 puncta, whereas $vps25^{A3/+}$ did not have a
229 significant effect (Figure 8A-D). The result indicates that, for exosome formation,
230 overexpression of *ifc* can overcome the requirement for *vps25* but not *hrs*. Because the
231 ESCRT-II complex is involved in the initiation of membrane invagination and the
232 recruitment of the ESCRT-III complex [ref], this finding supports a role for Ifc in the
233 early stage of membrane inward bending during ILV biogenesis.
234
235 <u>DEGS1 promotes the formation of ILVs *in vitro*</u>
236 To further evaluate if dhCer desaturase is sufficient to promote ILV formation, we
237 resorted to the *in vitro* model membrane system of GUV. After the generation of GUVs
238 using a mixture of dioleoylphophatidylcholine (DOPC) and cholesterol, we observed
239 whether there was spontaneous formation of ILVs over time. No ILV formation occurred
240 either with or without the inclusion of dhCer in the lipid mixture (Figure 9A,B-B',D-D').
241 Interestingly, when we added human DEGS1 recombinant protein to the GUVs with the
242 indicated lipid composition, we were able to observe the formation of ILVs in the GUVs
243 that containing dhCer but not without within 5 minutes (Figure 9A,C-C',E-E'). When we

244 added the DEGS1 inhibitor fenretinide to the system, the formation of ILVs induced by
245 DEGS1 was suppressed by fenretinide (Figure 9F,J-J'). The ethanol solvent control did
246 not inhibit ILV formation in the GUVs (Figure 9F,H-H'). The effect required the presence
247 of dhCer (Figure 9G-G', I-I'). These results show that the activity of DEGS1 was
248 required to promote the formation of ILV in the GUVs, likely by converting dhCer to Cer.
249 These data further support that the catalytic activity of DEGS1 promotes membrane
250 bending for the initiation of exosome biogenesis.
251
252
253 **Discussion**
254 In the present study, we developed an *in vivo* system for the analysis of exosome
255 production using *Drosophila* eye imaginal discs with the expression of GFP-CD63. We
256 showed that knocking out *ifc* in *Drosophila* eye imaginal discs reduced the production
257 and release of ELVs. In *ifc-KO*, the ELV marker CD63 became less associated with
258 endosomes but colocalized more with autophagosomes. On the contrary, transgenic
259 overexpression of *ifc(WT)-mCherry* promotes exosome biogenesis. In addition, our
260 genetic analysis and GUV assay support a role for Ifc in the early stage of ILV formation,
261 likely by regulating the invagination of the MVE membrane. We also showed that the
262 enzyme activity of DEGS1/Ifc is required to drive exosome formation since the
263 expression of a catalytic mutant form of *ifc* failed to promote exosome production and
264 inhibiting DEGS1 activity blocked ILV formation *in vitro*. Together, our data show that
265 DEGS1/Ifc promotes membrane invagination of ILV formation during exosome
266 biogenesis and controls the switch between exosome release and the autophagic

267 degradation of MVE, providing a mechanism for the cell non-autonomous function of
268 DEGS1/Ifc in the nervous system.
269
270 Between the ESCRT-dependent and Cer-mediated mechanisms of exosome
271 biogenesis, it is generally believed that the ESCRT-dependent mechanism is involved in
272 the selective sorting of cargos, whereas the Cer-dependent mechanisms are important to
273 control the initial membrane budding (Larios et al., 2020, Teis et al., 2010, Trajkovic et
274 al., 2008). However, *Kajimoto et al. (2013)* show that the continuous Cer catabolism
275 produces sphingosine 1-phosphate that is required for cargo sorting into ILVs in human
276 cells. Consistently, we found that *ifc-KO* reduced the localization of CD63-GFP to Rab5
277 in endosomes. While *in vitro* experiments demonstrated the ability of Cer to promote ILV
278 formation, the ESCRT-mediated and Cer-induced mechanisms are likely to be not
279 mutually exclusive of each other *in vivo*. Exosome membranes share similar lipid
280 composition with lipid rafts, both highly enriched for cholesterol and sphingolipids
281 (Hebbar et al., 2008). Lipid rafts are rigid membrane microdomains that serve as a
282 platform for protein-protein interaction and are essential for protein activation and signal
283 transduction (Lingwood and Simons, 2010). Cer-rich domains have been recognized to
284 affect raft properties by competing and displacing cholesterol (Megha and London,
285 2004). The Cer-rich membrane domains may not only serve as a permissive environment
286 to promote membrane invagination for ILV formation, but may also behave as a platform
287 to facilitate the segregation of exosome cargos. Our previous finding that Ifc resides in
288 endosomes also suggests that the on-site conversion of dhCer into Cer could regulate the
289 dynamic change of membrane property (Jung et al., 2017). Cer enrichment promotes the

290 formation of highly ordered gel phases and may induce the congregation of lipid rafts
291 into forming larger domains (Bieberich, 2018). The effects of dhCer accumulation on
292 cellular membranes need to be investigated to better elucidate the mechanism underlying
293 the systemic and peripheral neuropathies caused by human *DEGS1* deficiency.
294
295 Several previous studies have shown that inhibition of autophagosome-lysosome
296 degradation enhances exosome secretion (Danzer et al., 2012, Fader et al., 2008, Iguchi et
297 al., 2016). Interestingly, inhibition of autophagy by Bafilomycin A1 (BafA1) not only
298 increases the secretion of CD63+ exosomes but also increases the detection of autophagic
299 proteins p62 and LC3 in exosomes (Minakaki et al., 2018). However, autophagy proteins
300 ATG12–ATG3 have been shown to interact with the ESCRT-associated protein Alix to
301 promote late endosome to lysosome trafficking as well as exosome biogenesis (Murrow
302 et al., 2015). Also, knockout of ATG5 but not ATG7 significantly reduces the number of
303 exosomes, suggesting that not all of the autophagy core components participate in the
304 regulation of exosome release (Guo et al., 2017). In addition, exosomes purified from
305 cultured cortical neurons treated with BafA1 show a ~2-fold increase in certain
306 sphingolipid species, including Cer and dhCer, indicating BafA1 affects the lipid
307 composition of exosomes (Miranda et al., 2018). Leidal et al. (2020) report that LC3 and
308 LC3-conjugation machinery recruit specific cargos to pack into LC3-positive EVs for
309 secretion, a process which does not require the ESCRT complex but is dependent on the
310 activity of neutral sphingomyelinase 2, an enzyme which hydrolyzes sphingomyelin to
311 produced Cer. In the present study, we showed that exosome production increased with
312 the inhibition of autophagy by either 3-MA or chloroquine. However, combining

313 autophagy inhibition and *ifc* overexpression did not further increase exosome production,
314 suggesting *ifc* overexpression may inhibit autophagy. This is the opposite effect of *ifc-KO*
315 which induces autophagy. Together, these results suggest that the balance of dhCer and
316 Cer regulates the switch between autophagy and exosomes; further study is warranted to
317 elucidate the mechanism in detail.
318
319 While the effects of Cer have been extensively studied in various contexts, our
320 findings draw attention to the long-ignored sphingolipid species, dhCer. Although dhCer
321 is structurally different from Cer only in the lack of the 4,5-double bond, the two
322 sphingolipid species have widely different biophysical properties and bioactivities.
323 Several previous studies have hinted at a role for dhCer in the nervous system. Podbielska
324 et al. (2016) showed that treating human oligodendroglioma cells with inflammatory
325 cytokines greatly enhances the secretion of exosomes and significantly increases the
326 exosome and cellular levels of several sphingolipid species including dhCer.
327 Sphingolipidomics data from the Baltimore Longitudinal Study of Aging by following
328 992 cognitively normal individuals aged 55 years and older for an average of 15 years
329 concluded that plasma dhCer increase with age, but the trend was much steeper in women
330 than men and suggest dhCer may underlie the gender difference for degenerative diseases
331 such as Alzheimer's disease (Mielke et al., 2015). Fonteh et al. (2015) show that the level
332 of dhCer level in the cerebrospinal fluid increased significantly in patients with clinically
333 probable AD than it is in people with mild cognitive impairment, suggesting dhCer may
334 be used as an early marker for the progression to AD. Future studies are needed to
335 investigate whether the level and distribution of dhCer contribute to age-related

336 deterioration of the nervous system.

337

338

339 **Materials and Methods**

340 **Key Resources Table**

REAGENT or RESOURCE	SOURCE	IDENTIFIER
Antibodies		
Mouse anti-Na^+/K^+ ATPase	Developmental Studies Hybridoma Bank (DSHB)	Cat# a5; RRID: AB_2166869
Mouse anti-CD63		Cat# H5C6; RRID: AB_528158
Anti-Atg8a	Abcam	Cat# ab109364; RRID: AB_10861928
Anti-Rab5		Cat# ab31261; RRID: AB_882240
Alexa Fluor™ 647 Phalloidin	ThermoFisher	Cat# A22287; RRID: AB_2620155
DAPI		Cat# D1306; RRID: AB_2629482
Anti-RFP	Rockland	Cat# 600-401-379; RRID: AB_2209751
Anti-HA	Cell Signaling Technology	Cat# 3724; RRID:

		AB_1549585
Anti-mCherry	GeneTex	Cat# GTX630189
Anti-Actin	Millipore	Cat# MAB1501; RRID: AB_2223041
anti-mouse-HRP	Jackson ImmunoResearch Laboratories, Inc.	Cat# 115-005-003; RRID: AB_2338447
***Drosophila* Strains**		
ey3.5-FLP	Bloomington stock center (BDSC)	35542
cl, FRT40A		5622
FRT40A		5615
GMR>*w* RNAi		43344
DE-Gal4		29650
UAS-mCD8-GFP		5137
UAS-mCherry-CAAX		59021
UAS-hTSG101-HA		77977
rh1-Gal4, *ey*FLP		43347
UAS-Rab5CA		43335
nsyb-Gal4		5138
hrs^{D28}		54574
$vps25^{A3}$		39633
ifc-KO, FRT40A	Jung et al. (2017)	
UAS-*ifc*(WT)-mCherry		
UAS-EGFP-CD63	Gift from Dr. Suzanne Eaton	

	(Panakova et al., 2005)	
UAS-*ifc*(C1,2,3^{mut})-mCherry	This study	
UAS-Flo2-RFP	Bischoff et al. (2013)	
repo-FLP	Silies et al. (2007)	
repo-ifc-mCherry	This study	
Chemicals and other reagents		
DEGS1	Abcam	ab160100
Sucrose	Sigma	S7903
NaCl		31434
Glucose		G8270
NADPH		1010782400
ATP		A2383
$MgCl_2$	Calbiochem	442611

Lead Contact

Further information and requests for resources and reagents should be directed to and will be fulfilled by the Lead Contact, Shu-Yi Huang (shuyih@ntuh.gov.tw).

Materials Availability

All unique reagents generated in this study are available from the Lead Contact and may require completion of a Materials Transfer Agreement.

Experimental Model and Subject Details

351 ***Drosophila* strains and genetics**

352 *Drosophila* stocks were maintained at 25°C on standard medium and genetic crosses were
353 performed following standard fly husbandry procedures. Information on individual fly
354 strains can be found on FlyBase (flybase.org) unless otherwise noted in the above Key
355 Resources Table.

356

357 Eye-specific mosaic and whole-eye clones of *ifc-KO* were generated using the *ey-*
358 *FLP* system as previously described (Jung et al., 2017). The photoreceptor-specific *ey3.5-*
359 *FLP* was used to selectively create the homozygous *ifc* mutant clones in photoreceptors
360 (Mehta et al., 2005), whereas *repo-FLP* was used to generate glial-specific *ifc-KO* clones
361 (Silies et al., 2007). For light-stimulation experiments, a constant, 600 Lux LED light
362 source was provided for the indicated duration before the flies were used for
363 immunohistochemistry or electroretinogram

364

365 **Immunohistochemistry and confocal microscopy**

366 For immunofluorescence staining, larval eye discs and adult retina tissues were dissected,
367 fixed, washed, and immunostained with primary and secondary antibodies as previously
368 described (Jung et al., 2017). The antibodies used were listed in the above Key Resources
369 Table. All samples were mounted in Vectashield (Vector Laboratories) and analyzed on a
370 Carl Zeiss LSM880 confocal microscope with LAS AF software. Imaging data were
371 processed and quantified using Photoshop (CS6; Adobe), Illustrator (CS6; Adobe), and
372 ImageJ (National Institutes of Health).

373

374 **Electroretinogram**

375 Electroretinograms were performed, and the electric signals were amplified, filtered, and
376 recorded as previously described (Jung et al., 2017). To quantify the depolarization, all
377 experiments were carried out in triplicates with minimally 10 recordings per replicate for
378 each genotype and experimental condition.

379

380 **Site-directed mutagenesis of *UAS-ifc* mutants**

381 To generate point mutations in the catalytic domain of *UAS-ifc* transgene, the pUASt-ifc
382 was used as a backbone and site-directed mutagenesis was done with QuikChange Kit
383 (Agilent 200523) following the manufacturer's instruction. All constructs were verified
384 by sequencing. Transgenic flies were generated by embryo injection according to
385 standard protocols of integrase-mediated insertion (Bischof et al., 2007) followed by a
386 germline transmission screen.

387 Primer sequences:

ifc-C1^{mut}-FWD	GCCGAGATCTCGGCCAACCTGGCC
ifc-C1^{mut}-REV	GGCCGAGATCTCGGCAACGGCCAG
ifc-C2^{mut}-FWD	GCCCTGGAAGCCGCCCGTTACCAA
ifc-C2^{mut}-REV	GGCGGCTTCCAGGGCGTACTTTTT
ifc-C3^{mut}-FWD	GCCAACGAGGCCGCCGACTTTCCG
ifc-C3^{mut}-REV	GGCGGCCTCGTTGGCGTAGCCCAC
repo-ifc-mCherry-FWD	ATATGCGCGGCCGCCAAAATGGGACAGAAAGTTTC GCGCA
repo-ifc-mCherry-REV	CTAGTCTAGATTACTTGTACAGCTCGTCCATGCCGC

	CGGT

388

389 **Western blotting**

390 The protein extracts were prepared with dissected fly tissues that were homogenized for
391 10 min at 4°C in 1x RIPA buffer containing protease inhibitors (ThermoFisher A32955),
392 followed by centrifugation at 16000g for 15min at 4°C to remove the debris. The
393 supernatant of the homogenates was mixed with 4X sample buffer (20% glycerol, 4%
394 SDS, 100 mM Tris pH 6.8, 0.002% Bromophenol blue), boiled for 10 min, separated by
395 SDS-PAGE, and transferred in a wet-transfer tank to PVDF membranes (Millipore,
396 IPVH00010) following manufacturer's instructions (Bio-Rad). PVDF membranes were
397 incubated with 5% non-fat milk in TBST [10 mM Tris (pH 8.0), 150 mM NaCl, 0.1%
398 Tween 20] for 1 h at room temperature and then incubated with primary antibodies at 4°C
399 overnight. Membranes were then washed three times with TBST for 10 min each before
400 incubating with secondary antibodies in TBST for 1 h at room temperature, washed with
401 TBST three times, and developed with ECL reagents (Millipore, WBKLS0500). The
402 signals were captured by the BioSpectrum^{TM} 600 Imaging System (UVP Ltd), and the
403 relative intensities of bands were quantified by densitometry using the Image J software
404 (Schneider et al., 2012).

405

406 **Transmission electron microscopy and image analysis of MVE morphology**

407 Transmission electron microscopy was performed as previously described (Jung et al.,
408 2017). To characterize the MVE morphology, the fields of imaging for the
409 characterization within the eye of each genotype were selected randomly, and the image

410 files were blinded for the analyses of both the area of MVE and the number of ILV. The
411 area and number of MVE were quantified using Photoshop.
412
413 **Nanoparticle tracking analysis**
414 Fifty to 100 eye imaginal discs were dissected and incubated in sterile-filtered Schneider
415 medium (Gibco 21720024) with low-speed agitation (7 rpm) at room temperature for 2.5
416 h. The supernatant was then separated by low-speed centrifugation at 3,000 x g for 15
417 min to remove large debris, followed by another centrifugation at 12,000 x g for 15 min.
418 The samples were then passed through a Smart SEC single column (System Biosciences,
419 USA) for EV isolation. The size distribution was determined using NanoSight NS300
420 (Malvern Panalytical Ltd, United Kingdom) under constant flow condition (flow rate =
421 70) at 25°C. The recordings were analyzed by NTA 3.4 software Build 3.4.003 with the
422 detection threshold set to 6.
423
424 **Giant Unilamellar Vesicle (GUV) assay**
425 GUV was prepared by the electroformation method (Lee et al., 2018). Briefly, the lipid
426 mixture of Dioleoylphosphatidylcholine (DOPC) and cholesterol was dissolved in
427 chloroform at 1:0.67 molar ratio to the final concentration of 15mM. For lipid mixture
428 with dhCer, the lipid mixture included DOPC:dhCer:cholesterol at 1:1:0.67 molar ratio to
429 the total concentration of 15mM. The lipid mixture was then deposited into a chamber
430 made with a rubber O-ring on an electrically conductive ITO glass. The setup was
431 vacuum dried at 50°C for 1 h, and the solvent was evaporated thereby producing a thin
432 lipid film. The chamber was then re-filled with 2ml of 400mM sucrose. Depending on the

433 experimental conditions, 0.2 μM of the DEGS1 inhibitor fenretinide might be added to
434 the sucrose solution. After sealing the chamber with another piece of ITO glass, the setup
435 was supplied with a sinusoidal voltage waveform of 3.5 V amplitude at 10 Hz frequency
436 and kept at 65°C overnight. The unilamellar vesicles were cooled down and resuspended
437 in 200 μl of 400mM glucose, and confocal images were acquired using Zeiss Cell
438 Observer SD to show the morphology of GUV at time = 0. The recombinant DEGS1
439 protein at the concentration of 9.62 nM and co-factors (ATP 4 mM, NADPH 2 mM,
440 MgCl2 2.4 mM, NaCl 50 mM, and sucrose 50 mM) were then supplemented to the
441 GUV/sucrose mixture. The post-treatment images were acquired after 5 min of
442 incubation at 37°C.
443
444 **Quantification and statistical analysis**
445 Quantitative data were analyzed using a two-tailed unpaired Student's *t*-test or one-way
446 ANOVA with Tukey's multiple comparison test. Data analysis was performed using
447 GraphPad Prism 5. All data in bar graphs are shown as mean ± SEM. The quantified
448 GFP-CD63 puncta in the experimental groups were normalized to the average of the
449 controls which was set as 1. *P* values of less than 0.05 were regarded as statistically
450 significant. All quantifications included at least three experimental replicates.
451
452
453 **Acknowledgements**
454 The authors are grateful to Drs. Guang-Chao Chen, Robin Hiesinger, Jennifer Jin, Ya-
455 Wen Liu, Yi Henry Sun, Chao-Wen Wang, Chi-Kuang Yao, and Mr. Fei-Yang Tzou for

their comments on the manuscript. The authors sincerely thank Dr. Ya-Wen Liu and Ms. Yu-Chen Chang for helping us established the GUV system. We thank the staff of the Imaging Core at the First Core Lab, National Taiwan University College of Medicine, and the staff of the Second Core Lab, Department of Medical Research, National Taiwan University Hospital for technical support. We thank the staff of the Electron Microscopy Laboratory, Tzu Chi University, for technical support in TEM. We thank WellGenetics, Inc. for embryo injection service. Stocks obtained from the Bloomington Drosophila Stock Center (NIH P40OD018537) were used in this study. This work was supported by the Ministry of Science and Technology of Taiwan grants 107WFA0111977 to S.-Y. Huang and 108-2311-B-002-011-MY3, National Taiwan University Hospital grant 109-21 to S.-Y. Huang, and by National Taiwan University grant 109L104308 to C-C Chan.

Declaration of interests

The authors declare no competing financial interests.

Abbreviations

Cer, ceramide;

dhCer, dihydroceramide;

ELVs, exosome-like vesicles;

ESCRT, Endosomal Sorting Complexes Required for Transport;

ERG, electroretinogram;

GUV, giant unilamellar vesicles;

ILVs, intraluminal vesicles;

479 MVEs, multivesicular endosomes.

480

481

482 **References**

483 Adell, M. A., Vogel, G. F., Pakdel, M., Muller, M., Lindner, H., Hess, M. W. & Teis, D.
484 2014. Coordinated binding of Vps4 to ESCRT-III drives membrane neck
485 constriction during MVB vesicle formation. *J Cell Biol,* 205**,** 33-49. DOI:
486 https://doi.org/10.1083/jcb.201310114.
487 Barbarroja, N., Rodriguez-Cuenca, S., Nygren, H., Camargo, A., Pirraco, A., Relat, J.,
488 Cuadrado, I., Pellegrinelli, V., Medina-Gomez, G., Lopez-Pedrera, C., Tinahones,
489 F. J., Symons, J. D., Summers, S. A., Oresic, M. & Vidal-Puig, A. 2015. Increased
490 dihydroceramide/ceramide ratio mediated by defective expression of degs1
491 impairs adipocyte differentiation and function. *Diabetes,* 64**,** 1180-92. DOI:
492 https://doi.org/10.2337/db14-0359.
493 Bieberich, E. 2018. Sphingolipids and lipid rafts: Novel concepts and methods of
494 analysis. *Chem Phys Lipids,* 216**,** 114-131. DOI:
495 https://doi.org/10.1016/j.chemphyslip.2018.08.003.
496 Bischof, J., Maeda, R. K., Hediger, M., Karch, F. & Basler, K. 2007. An optimized
497 transgenesis system for Drosophila using germ-line-specific phiC31 integrases.
498 *Proc Natl Acad Sci U S A,* 104**,** 3312-7. DOI:
499 https://doi.org/10.1073/pnas.0611511104.
500 Bischoff, M., Gradilla, A. C., Seijo, I., Andres, G., Rodriguez-Navas, C., Gonzalez-
501 Mendez, L. & Guerrero, I. 2013. Cytonemes are required for the establishment of
502 a normal Hedgehog morphogen gradient in Drosophila epithelia. *Nat Cell Biol,*
503 15**,** 1269-81. DOI: https://doi.org/10.1038/ncb2856.
504 Brzozowski, J. S., Jankowski, H., Bond, D. R., Mccague, S. B., Munro, B. R., Predebon,
505 M. J., Scarlett, C. J., Skelding, K. A. & Weidenhofer, J. 2018. Lipidomic profiling
506 of extracellular vesicles derived from prostate and prostate cancer cell lines.
507 *Lipids Health Dis,* 17**,** 211. DOI: https://doi.org/10.1186/s12944-018-0854-x.
508 Budnik, V., Ruiz-Canada, C. & Wendler, F. 2016. Extracellular vesicles round off
509 communication in the nervous system. *Nat Rev Neurosci,* 17**,** 160-72. DOI:
510 https://doi.org/10.1038/nrn.2015.29.
511 Buono, R. A., Leier, A., Paez-Valencia, J., Pennington, J., Goodman, K., Miller, N.,
512 Ahlquist, P., Marquez-Lago, T. T. & Otegui, M. S. 2017. ESCRT-mediated vesicle
513 concatenation in plant endosomes. *J Cell Biol,* 216**,** 2167-2177. DOI:
514 https://doi.org/10.1083/jcb.201612040.
515 Danzer, K. M., Kranich, L. R., Ruf, W. P., Cagsal-Getkin, O., Winslow, A. R., Zhu, L.,
516 Vanderburg, C. R. & Mclean, P. J. 2012. Exosomal cell-to-cell transmission of
517 alpha synuclein oligomers. *Mol Neurodegener,* 7**,** 42. DOI:
518 https://doi.org/10.1186/1750-1326-7-42.
519 Dolgin, V., Straussberg, R., Xu, R., Mileva, I., Yogev, Y., Khoury, R., Konen, O., Barhum,
520 Y., Zvulunov, A., Mao, C. & Birk, O. S. 2019. DEGS1 variant causes neurological

521 disorder. *Eur J Hum Genet,* 27**,** 1668-1676. DOI: https://doi.org/10.1038/s41431-
522 019-0444-z.
523 Fader, C. M., Sanchez, D., Furlan, M. & Colombo, M. I. 2008. Induction of autophagy
524 promotes fusion of multivesicular bodies with autophagic vacuoles in k562 cells.
525 *Traffic,* 9**,** 230-50. DOI: https://doi.org/10.1111/j.1600-0854.2007.00677.x.
526 Flores, I., Martinez, A. C., Hannun, Y. A. & Merida, I. 1998. Dual role of ceramide in the
527 control of apoptosis following IL-2 withdrawal. *J Immunol,* 160**,** 3528-33.
528 Fonteh, A. N., Ormseth, C., Chiang, J., Cipolla, M., Arakaki, X. & Harrington, M. G.
529 2015. Sphingolipid metabolism correlates with cerebrospinal fluid Beta amyloid
530 levels in Alzheimer's disease. *PLoS One,* 10**,** e0125597. DOI:
531 https://doi.org/10.1371/journal.pone.0125597.
532 Gagliostro, V., Casas, J., Caretti, A., Abad, J. L., Tagliavacca, L., Ghidoni, R., Fabrias, G.
533 & Signorelli, P. 2012. Dihydroceramide delays cell cycle G1/S transition via
534 activation of ER stress and induction of autophagy. *Int J Biochem Cell Biol,* 44**,**
535 2135-43. DOI: https://doi.org/10.1016/j.biocel.2012.08.025.
536 Gross, J. C., Chaudhary, V., Bartscherer, K. & Boutros, M. 2012. Active Wnt proteins are
537 secreted on exosomes. *Nat Cell Biol,* 14**,** 1036-45. DOI:
538 https://doi.org/10.1038/ncb2574.
539 Guo, H., Chitiprolu, M., Roncevic, L., Javalet, C., Hemming, F. J., Trung, M. T., Meng,
540 L., Latreille, E., Tanese De Souza, C., Mcculloch, D., Baldwin, R. M., Auer, R.,
541 Cote, J., Russell, R. C., Sadoul, R. & Gibbings, D. 2017. Atg5 Disassociates the
542 V1V0-ATPase to Promote Exosome Production and Tumor Metastasis
543 Independent of Canonical Macroautophagy. *Dev Cell,* 43**,** 716-730 e7. DOI:
544 https://doi.org/10.1016/j.devcel.2017.11.018.
545 Hebbar, S., Lee, E., Manna, M., Steinert, S., Kumar, G. S., Wenk, M., Wohland, T. &
546 Kraut, R. 2008. A fluorescent sphingolipid binding domain peptide probe interacts
547 with sphingolipids and cholesterol-dependent raft domains. *J Lipid Res,* 49**,** 1077-
548 89. DOI: https://doi.org/10.1194/jlr.M700543-JLR200.
549 Hernandez-Tiedra, S., Fabrias, G., Davila, D., Salanueva, I. J., Casas, J., Montes, L. R.,
550 Anton, Z., Garcia-Taboada, E., Salazar-Roa, M., Lorente, M., Nylandsted, J.,
551 Armstrong, J., Lopez-Valero, I., Mckee, C. S., Serrano-Puebla, A., Garcia-Lopez,
552 R., Gonzalez-Martinez, J., Abad, J. L., Hanada, K., Boya, P., Goni, F., Guzman,
553 M., Lovat, P., Jaattela, M., Alonso, A. & Velasco, G. 2016. Dihydroceramide
554 accumulation mediates cytotoxic autophagy of cancer cells via autolysosome
555 destabilization. *Autophagy,* 12**,** 2213-2229. DOI:
556 https://doi.org/10.1080/15548627.2016.1213927.
557 Holland, W. L., Brozinick, J. T., Wang, L. P., Hawkins, E. D., Sargent, K. M., Liu, Y.,
558 Narra, K., Hoehn, K. L., Knotts, T. A., Siesky, A., Nelson, D. H., Karathanasis, S.
559 K., Fontenot, G. K., Birnbaum, M. J. & Summers, S. A. 2007. Inhibition of
560 ceramide synthesis ameliorates glucocorticoid-, saturated-fat-, and obesity-
561 induced insulin resistance. *Cell Metab,* 5**,** 167-79. DOI:
562 https://doi.org/10.1016/j.cmet.2007.01.002.
563 Iguchi, Y., Eid, L., Parent, M., Soucy, G., Bareil, C., Riku, Y., Kawai, K., Takagi, S.,
564 Yoshida, M., Katsuno, M., Sobue, G. & Julien, J. P. 2016. Exosome secretion is a
565 key pathway for clearance of pathological TDP-43. *Brain,* 139**,** 3187-3201. DOI:
566 https://doi.org/10.1093/brain/aww237.

567 Jung, W. H., Liu, C. C., Yu, Y. L., Chang, Y. C., Lien, W. Y., Chao, H. C., Huang, S. Y.,
568 Kuo, C. H., Ho, H. C. & Chan, C. C. 2017. Lipophagy prevents activity-
569 dependent neurodegeneration due to dihydroceramide accumulation in vivo.
570 *EMBO Rep,* 18**,** 1150-1165. DOI: https://doi.org/10.15252/embr.201643480.
571 Kajimoto, T., Okada, T., Miya, S., Zhang, L. & Nakamura, S. 2013. Ongoing activation
572 of sphingosine 1-phosphate receptors mediates maturation of exosomal
573 multivesicular endosomes. *Nat Commun,* 4**,** 2712. DOI:
574 https://doi.org/10.1038/ncomms3712.
575 Karsai, G., Kraft, F., Haag, N., Korenke, G. C., Hanisch, B., Othman, A.,
576 Suriyanarayanan, S., Steiner, R., Knopp, C., Mull, M., Bergmann, M., Schroder, J.
577 M., Weis, J., Elbracht, M., Begemann, M., Hornemann, T. & Kurth, I. 2019.
578 DEGS1-associated aberrant sphingolipid metabolism impairs nervous system
579 function in humans. *J Clin Invest,* 129**,** 1229-1239. DOI:
580 https://doi.org/10.1172/JCI124159.
581 Katzmann, D. J., Babst, M. & Emr, S. D. 2001. Ubiquitin-dependent sorting into the
582 multivesicular body pathway requires the function of a conserved endosomal
583 protein sorting complex, ESCRT-I. *Cell,* 106**,** 145-55. DOI:
584 https://doi.org/10.1016/s0092-8674(01)00434-2.
585 Kraveka, J. M., Li, L., Szulc, Z. M., Bielawski, J., Ogretmen, B., Hannun, Y. A., Obeid,
586 L. M. & Bielawska, A. 2007. Involvement of dihydroceramide desaturase in cell
587 cycle progression in human neuroblastoma cells. *J Biol Chem,* 282**,** 16718-28.
588 DOI: https://doi.org/10.1074/jbc.M700647200.
589 Larios, J., Mercier, V., Roux, A. & Gruenberg, J. 2020. ALIX- and ESCRT-III-dependent
590 sorting of tetraspanins to exosomes. *J Cell Biol,* 219. DOI:
591 https://doi.org/10.1083/jcb.201904113.
592 Lee, C. W., Chiang, Y. L., Liu, J. T., Chen, Y. X., Lee, C. H., Chen, Y. L. & Hwang, I. S.
593 2018. Emerging Roles of Air Gases in Lipid Bilayers. *Small,* 14**,** e1802133. DOI:
594 https://doi.org/10.1002/smll.201802133.
595 Lee, S. Y., Kim, J. R., Hu, Y., Khan, R., Kim, S. J., Bharadwaj, K. G., Davidson, M. M.,
596 Choi, C. S., Shin, K. O., Lee, Y. M., Park, W. J., Park, I. S., Jiang, X. C.,
597 Goldberg, I. J. & Park, T. S. 2012. Cardiomyocyte specific deficiency of serine
598 palmitoyltransferase subunit 2 reduces ceramide but leads to cardiac dysfunction.
599 *J Biol Chem,* 287**,** 18429-39. DOI: https://doi.org/10.1074/jbc.M111.296947.
600 Leidal, A. M., Huang, H. H., Marsh, T., Solvik, T., Zhang, D., Ye, J., Kai, F., Goldsmith,
601 J., Liu, J. Y., Huang, Y. H., Monkkonen, T., Vlahakis, A., Huang, E. J., Goodarzi,
602 H., Yu, L., Wiita, A. P. & Debnath, J. 2020. The LC3-conjugation machinery
603 specifies the loading of RNA-binding proteins into extracellular vesicles. *Nat Cell*
604 *Biol,* 22**,** 187-199. DOI: https://doi.org/10.1038/s41556-019-0450-y.
605 Li, L., Tang, X., Taylor, K. G., Dupre, D. B. & Yappert, M. C. 2002. Conformational
606 characterization of ceramides by nuclear magnetic resonance spectroscopy.
607 *Biophys J,* 82**,** 2067-80. DOI: https://doi.org/10.1016/S0006-3495(02)75554-9.
608 Lingwood, D. & Simons, K. 2010. Lipid rafts as a membrane-organizing principle.
609 *Science,* 327**,** 46-50. DOI: https://doi.org/10.1126/science.1174621.
610 Lloyd, T. E., Atkinson, R., Wu, M. N., Zhou, Y., Pennetta, G. & Bellen, H. J. 2002. Hrs
611 regulates endosome membrane invagination and tyrosine kinase receptor
612 signaling in Drosophila. *Cell,* 108**,** 261-9. DOI: https://doi.org/10.1016/s0092-

613 8674(02)00611-6.
614 Megha & London, E. 2004. Ceramide selectively displaces cholesterol from ordered lipid
615 domains (rafts): implications for lipid raft structure and function. *J Biol Chem,*
616 279**,** 9997-10004. DOI: https://doi.org/10.1074/jbc.M309992200.
617 Mehta, S. Q., Hiesinger, P. R., Beronja, S., Zhai, R. G., Schulze, K. L., Verstreken, P.,
618 Cao, Y., Zhou, Y., Tepass, U., Crair, M. C. & Bellen, H. J. 2005. Mutations in
619 Drosophila sec15 reveal a function in neuronal targeting for a subset of exocyst
620 components. *Neuron,* 46**,** 219-32. DOI:
621 https://doi.org/10.1016/j.neuron.2005.02.029.
622 Mielke, M. M., Bandaru, V. V., Han, D., An, Y., Resnick, S. M., Ferrucci, L. & Haughey,
623 N. J. 2015. Demographic and clinical variables affecting mid- to late-life
624 trajectories of plasma ceramide and dihydroceramide species. *Aging Cell,* 14**,**
625 1014-23. DOI: https://doi.org/10.1111/acel.12369.
626 Minakaki, G., Menges, S., Kittel, A., Emmanouilidou, E., Schaeffner, I., Barkovits, K.,
627 Bergmann, A., Rockenstein, E., Adame, A., Marxreiter, F., Mollenhauer, B.,
628 Galasko, D., Buzas, E. I., Schlotzer-Schrehardt, U., Marcus, K., Xiang, W., Lie,
629 D. C., Vekrellis, K., Masliah, E., Winkler, J. & Klucken, J. 2018. Autophagy
630 inhibition promotes SNCA/alpha-synuclein release and transfer via extracellular
631 vesicles with a hybrid autophagosome-exosome-like phenotype. *Autophagy,* 14**,**
632 98-119. DOI: https://doi.org/10.1080/15548627.2017.1395992.
633 Miranda, A. M., Lasiecka, Z. M., Xu, Y., Neufeld, J., Shahriar, S., Simoes, S., Chan, R.
634 B., Oliveira, T. G., Small, S. A. & Di Paolo, G. 2018. Neuronal lysosomal
635 dysfunction releases exosomes harboring APP C-terminal fragments and unique
636 lipid signatures. *Nat Commun,* 9**,** 291. DOI: https://doi.org/10.1038/s41467-017-
637 02533-w.
638 Morrison, C. M. & Halder, G. 2010. Characterization of a dorsal-eye Gal4 Line in
639 Drosophila. *Genesis,* 48**,** 3-7. DOI: https://doi.org/10.1002/dvg.20571.
640 Munoz-Guardiola, P., Casas, J., Megias-Roda, E., Sole, S., Perez-Montoyo, H., Yeste-
641 Velasco, M., Erazo, T., Dieguez-Martinez, N., Espinosa-Gil, S., Munoz-Pinedo,
642 C., Yoldi, G., Abad, J. L., Segura, M. F., Moran, T., Romeo, M., Bosch-Barrera, J.,
643 Oaknin, A., Alfon, J., Domenech, C., Fabrias, G., Velasco, G. & Lizcano, J. M.
644 2020. The anti-cancer drug ABTL0812 induces ER stress-mediated cytotoxic
645 autophagy by increasing dihydroceramide levels in cancer cells. *Autophagy***,** 1-18.
646 DOI: https://doi.org/10.1080/15548627.2020.1761651.
647 Murrow, L., Malhotra, R. & Debnath, J. 2015. ATG12-ATG3 interacts with Alix to
648 promote basal autophagic flux and late endosome function. *Nat Cell Biol,* 17**,** 300-
649 10. DOI: https://doi.org/10.1038/ncb3112.
650 Panakova, D., Sprong, H., Marois, E., Thiele, C. & Eaton, S. 2005. Lipoprotein particles
651 are required for Hedgehog and Wingless signalling. *Nature,* 435**,** 58-65. DOI:
652 https://doi.org/10.1038/nature03504.
653 Pant, D. C., Dorboz, I., Schluter, A., Fourcade, S., Launay, N., Joya, J., Aguilera-Albesa,
654 S., Yoldi, M. E., Casasnovas, C., Willis, M. J., Ruiz, M., Ville, D., Lesca, G.,
655 Siquier-Pernet, K., Desguerre, I., Yan, H., Wang, J., Burmeister, M., Brady, L.,
656 Tarnopolsky, M., Cornet, C., Rubbini, D., Terriente, J., James, K. N., Musaev, D.,
657 Zaki, M. S., Patterson, M. C., Lanpher, B. C., Klee, E. W., Pinto, E. V. F., Wohler,
658 E., Sobreira, N. L. M., Cohen, J. S., Maroofian, R., Galehdari, H., Mazaheri, N.,

659 Shariati, G., Colleaux, L., Rodriguez, D., Gleeson, J. G., Pujades, C., Fatemi, A.,
660 Boespflug-Tanguy, O. & Pujol, A. 2019. Loss of the sphingolipid desaturase
661 DEGS1 causes hypomyelinating leukodystrophy. *J Clin Invest,* 129**,** 1240-1256.
662 DOI: https://doi.org/10.1172/JCI123959.
663 Podbielska, M., Szulc, Z. M., Kurowska, E., Hogan, E. L., Bielawski, J., Bielawska, A. &
664 Bhat, N. R. 2016. Cytokine-induced release of ceramide-enriched exosomes as a
665 mediator of cell death signaling in an oligodendroglioma cell line. *J Lipid Res,* 57**,**
666 2028-2039. DOI: https://doi.org/10.1194/jlr.M070664.
667 Poehler, A. M., Xiang, W., Spitzer, P., May, V. E., Meixner, H., Rockenstein, E., Chutna,
668 O., Outeiro, T. F., Winkler, J., Masliah, E. & Klucken, J. 2014. Autophagy
669 modulates SNCA/alpha-synuclein release, thereby generating a hostile
670 microenvironment. *Autophagy,* 10**,** 2171-92. DOI:
671 https://doi.org/10.4161/auto.36436.
672 Raposo, G. & Stoorvogel, W. 2013. Extracellular vesicles: exosomes, microvesicles, and
673 friends. *J Cell Biol,* 200**,** 373-83. DOI: https://doi.org/10.1083/jcb.201211138.
674 Schneider, C. A., Rasband, W. S. & Eliceiri, K. W. 2012. NIH Image to ImageJ: 25 years
675 of image analysis. *Nat Methods,* 9**,** 671-5. DOI:
676 https://doi.org/10.1038/nmeth.2089.
677 Siddique, M. M., Li, Y., Wang, L., Ching, J., Mal, M., Ilkayeva, O., Wu, Y. J., Bay, B. H.
678 & Summers, S. A. 2013. Ablation of dihydroceramide desaturase 1, a therapeutic
679 target for the treatment of metabolic diseases, simultaneously stimulates anabolic
680 and catabolic signaling. *Mol Cell Biol,* 33**,** 2353-69. DOI:
681 https://doi.org/10.1128/MCB.00226-13.
682 Silies, M., Yuva, Y., Engelen, D., Aho, A., Stork, T. & Klambt, C. 2007. Glial cell
683 migration in the eye disc. *J Neurosci,* 27**,** 13130-9. DOI:
684 https://doi.org/10.1523/JNEUROSCI.3583-07.2007.
685 Stenmark, H., Parton, R. G., Steele-Mortimer, O., Lutcke, A., Gruenberg, J. & Zerial, M.
686 1994. Inhibition of rab5 GTPase activity stimulates membrane fusion in
687 endocytosis. *EMBO J,* 13**,** 1287-96.
688 Tang, Y., Cai, Q. H., Wang, Y. J., Fan, S. H., Zhang, Z. F., Xiao, M. Q., Zhu, J. Y., Wu, D.
689 M., Lu, J. & Zheng, Y. L. 2017. Protective effect of autophagy on endoplasmic
690 reticulum stress induced apoptosis of alveolar epithelial cells in rat models of
691 COPD. *Biosci Rep,* 37. DOI: https://doi.org/10.1042/BSR20170803.
692 Teis, D., Saksena, S., Judson, B. L. & Emr, S. D. 2010. ESCRT-II coordinates the
693 assembly of ESCRT-III filaments for cargo sorting and multivesicular body
694 vesicle formation. *EMBO J,* 29**,** 871-83. DOI:
695 https://doi.org/10.1038/emboj.2009.408.
696 Ternes, P., Franke, S., Zahringer, U., Sperling, P. & Heinz, E. 2002. Identification and
697 characterization of a sphingolipid delta 4-desaturase family. *J Biol Chem,* 277**,**
698 25512-8. DOI: https://doi.org/10.1074/jbc.M202947200.
699 Thery, C., Boussac, M., Veron, P., Ricciardi-Castagnoli, P., Raposo, G., Garin, J. &
700 Amigorena, S. 2001. Proteomic analysis of dendritic cell-derived exosomes: a
701 secreted subcellular compartment distinct from apoptotic vesicles. *J Immunol,*
702 166**,** 7309-18. DOI: https://doi.org/10.4049/jimmunol.166.12.7309.
703 Thery, C., Witwer, K. W., Aikawa, E., Alcaraz, M. J., Anderson, J. D., Andriantsitohaina,
704 R., Antoniou, A., Arab, T., Archer, F., Atkin-Smith, G. K., Ayre, D. C., Bach, J.

705 M., Bachurski, D., Baharvand, H., Balaj, L., Baldacchino, S., Bauer, N. N.,
706 Baxter, A. A., Bebawy, M., Beckham, C., Bedina Zavec, A., Benmoussa, A.,
707 Berardi, A. C., Bergese, P., Bielska, E., Blenkiron, C., Bobis-Wozowicz, S.,
708 Boilard, E., Boireau, W., Bongiovanni, A., Borras, F. E., Bosch, S., Boulanger, C.
709 M., Breakefield, X., Breglio, A. M., Brennan, M. A., Brigstock, D. R., Brisson,
710 A., Broekman, M. L., Bromberg, J. F., Bryl-Gorecka, P., Buch, S., Buck, A. H.,
711 Burger, D., Busatto, S., Buschmann, D., Bussolati, B., Buzas, E. I., Byrd, J. B.,
712 Camussi, G., Carter, D. R., Caruso, S., Chamley, L. W., Chang, Y. T., Chen, C.,
713 Chen, S., Cheng, L., Chin, A. R., Clayton, A., Clerici, S. P., Cocks, A., Cocucci,
714 E., Coffey, R. J., Cordeiro-Da-Silva, A., Couch, Y., Coumans, F. A., Coyle, B.,
715 Crescitelli, R., Criado, M. F., D'souza-Schorey, C., Das, S., Datta Chaudhuri, A.,
716 De Candia, P., De Santana, E. F., De Wever, O., Del Portillo, H. A., Demaret, T.,
717 Deville, S., Devitt, A., Dhondt, B., Di Vizio, D., Dieterich, L. C., Dolo, V.,
718 Dominguez Rubio, A. P., Dominici, M., Dourado, M. R., Driedonks, T. A., Duarte,
719 F. V., Duncan, H. M., Eichenberger, R. M., Ekstrom, K., El Andaloussi, S., Elie-
720 Caille, C., Erdbrugger, U., Falcon-Perez, J. M., Fatima, F., Fish, J. E., Flores-
721 Bellver, M., Forsonits, A., Frelet-Barrand, A., et al. 2018. Minimal information for
722 studies of extracellular vesicles 2018 (MISEV2018): a position statement of the
723 International Society for Extracellular Vesicles and update of the MISEV2014
724 guidelines. *J Extracell Vesicles,* 7**,** 1535750. DOI:
725 https://doi.org/10.1080/20013078.2018.1535750.
726 Trajkovic, K., Hsu, C., Chiantia, S., Rajendran, L., Wenzel, D., Wieland, F., Schwille, P.,
727 Brugger, B. & Simons, M. 2008. Ceramide triggers budding of exosome vesicles
728 into multivesicular endosomes. *Science,* 319**,** 1244-7. DOI:
729 https://doi.org/10.1126/science.1153124.
730 Vaccari, T. & Bilder, D. 2005. The Drosophila tumor suppressor vps25 prevents
731 nonautonomous overproliferation by regulating notch trafficking. *Dev Cell,* 9**,**
732 687-98. DOI: https://doi.org/10.1016/j.devcel.2005.09.019.
733 Vallabhaneni, K. C., Penfornis, P., Dhule, S., Guillonneau, F., Adams, K. V., Mo, Y. Y.,
734 Xu, R., Liu, Y., Watabe, K., Vemuri, M. C. & Pochampally, R. 2015. Extracellular
735 vesicles from bone marrow mesenchymal stem/stromal cells transport tumor
736 regulatory microRNA, proteins, and metabolites. *Oncotarget,* 6**,** 4953-67. DOI:
737 https://doi.org/10.18632/oncotarget.3211.
738 Van Meer, G., Voelker, D. R. & Feigenson, G. W. 2008. Membrane lipids: where they are
739 and how they behave. *Nat Rev Mol Cell Biol,* 9**,** 112-24. DOI:
740 https://doi.org/10.1038/nrm2330.
741 Vidal, M. J. & Stahl, P. D. 1993. The small GTP-binding proteins Rab4 and ARF are
742 associated with released exosomes during reticulocyte maturation. *Eur J Cell*
743 *Biol,* 60**,** 261-7.
744 Villarroya-Beltri, C., Baixauli, F., Mittelbrunn, M., Fernandez-Delgado, I., Torralba, D.,
745 Moreno-Gonzalo, O., Baldanta, S., Enrich, C., Guerra, S. & Sanchez-Madrid, F.
746 2016. ISGylation controls exosome secretion by promoting lysosomal degradation
747 of MVB proteins. *Nat Commun,* 7**,** 13588. DOI:
748 https://doi.org/10.1038/ncomms13588.
749 Wegner, C. S., Malerod, L., Pedersen, N. M., Progida, C., Bakke, O., Stenmark, H. &
750 Brech, A. 2010. Ultrastructural characterization of giant endosomes induced by

751 GTPase-deficient Rab5. *Histochem Cell Biol,* 133**,** 41-55. DOI:
752 https://doi.org/10.1007/s00418-009-0643-8.
753 Xiong, W. C. & Montell, C. 1995. Defective glia induce neuronal apoptosis in the repo
754 visual system of Drosophila. *Neuron,* 14**,** 581-90. DOI:
755 https://doi.org/10.1016/0896-6273(95)90314-3.
756

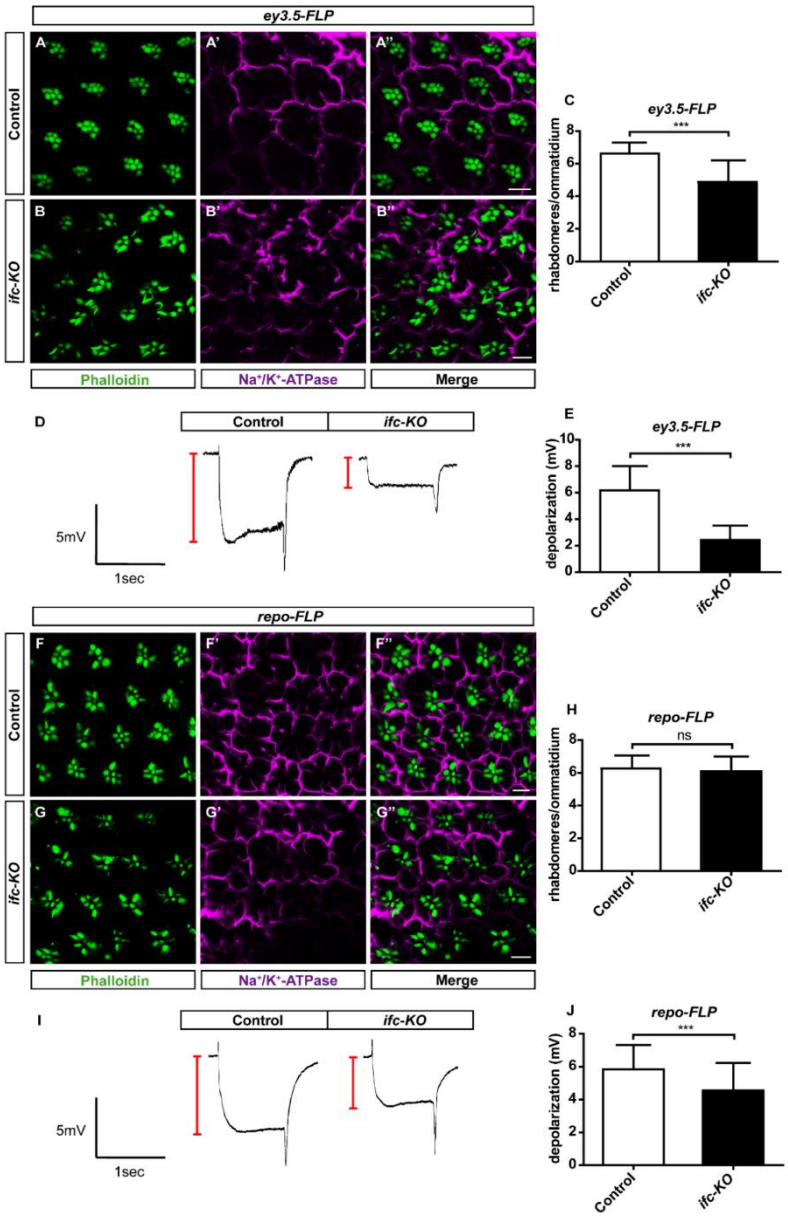

Figure 1.Tissue-specific requirements for *ifc-KO* in *Drosophila* photoreceptors and the surrounding glia. (A and B) Representative confocal images showing ommatidial morphology after 10 days of light stimulation in the control (A) and *ey3.5-FLP*-induced *ifc-KO* (B). Scale bar = 10 µm. **(C)** Quantification of rhabdomeres per ommatidium. **(D)** Representative electroretinogram (ERG) traces. **(E)** Quantification of the depolarization amplitudes of ERG. **(F and G)** Representative confocal images of the control (F) and *repo-FLP*-induced *ifc-KO* in glia (G). **(H)** Quantification of rhabdomeres per ommatidium. **(I)** Representative ERG traces. **(J)** Quantification of ERG depolarization amplitudes after 10 days of light stimulation. Phalloidin shows rhabdomeres in green; anti-Na+/K+-ATPase shows neuronal membrane in magenta. Bar charts show mean ± SEM of at least three independent experiments. *** $p < 0.001$, ns: Not significant (Student's *t*-test).

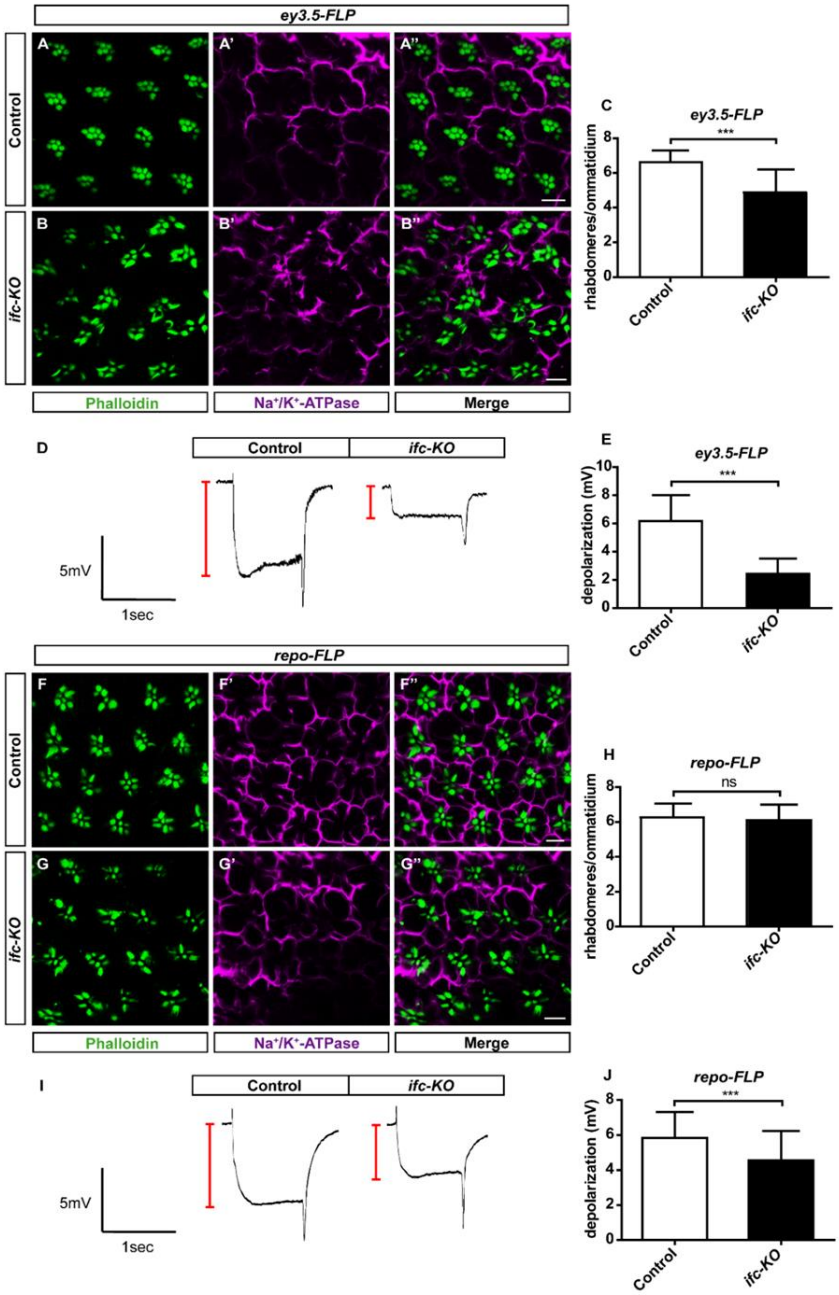

Figure 2. Cell non-autonomous rescue of *ifc-KO* eye clones. (A-C) Representative confocal images of ommatidial morphology of *ifc-KO* whole eye clones created by *ey-FLP* (A-A'') and *ifc-KO* with eye expression of *ifc(WT)-mCherry* driven by *GMR-Gal4* (B-B'') or *ifc(WT)-mCherry* in the glia under *repo-Gal4* (C-C'') after 10 days of light stimulation. Phalloidin staining shows rhabdomere in green and anti-Na+/K+-ATPase shows neuronal membrane in magenta. Scale bars: 10 µm. **(D)** Quantification of rhabdomeres per ommatidium. **(E)** Representative electroretinogram (ERG) traces after 10 days of light stimulation. **(F)** Quantification of the depolarization amplitudes of ERG. Bar charts show mean ± SEM of at least three independent experiments. ***P < 0.001 (Student's *t*-test).

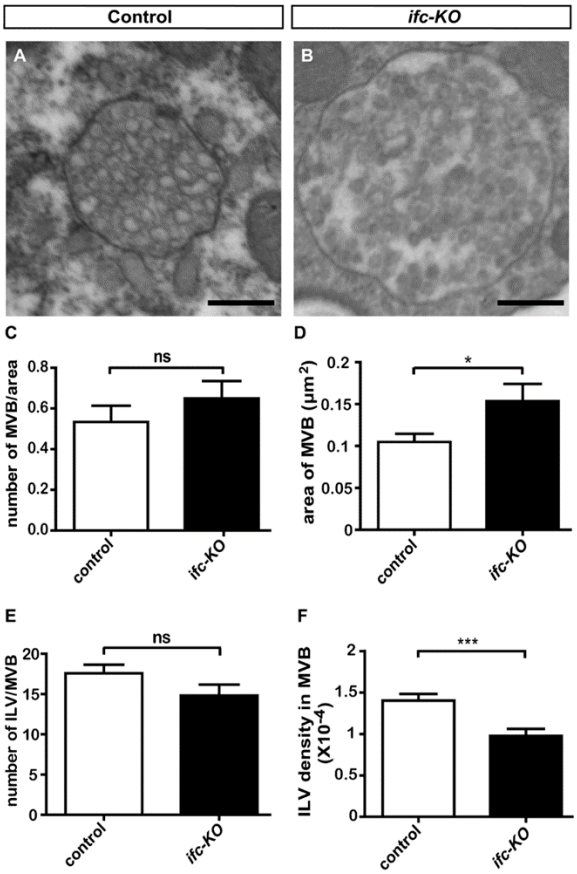

Figure 3. Knocking-out ifc reduces the density of intraluminal vesicles (ILVs) inside of multivesicular endosomes (MVEs) in *Drosophila* photoreceptors. (A and B) Representative transmission electron microscopy (TEM) images of the control (A) and *ifc-KO* eyes (B) after 3 days of light stimulation. Scale bars: 250 nm. **(C)** Quantification of the number of MVEs per field. **(D)** Quantification of the area of MVEs. **(E)** Quantification of the number of ILVs per MVE. **(F)** Quantification of the number of ILVs per unit area inside MVEs. Bar charts show mean ± SEM of at least three independent experiments. *** $p < 0.001$, * $p < 0.05$, ns: Not significant (Student's *t*-test).

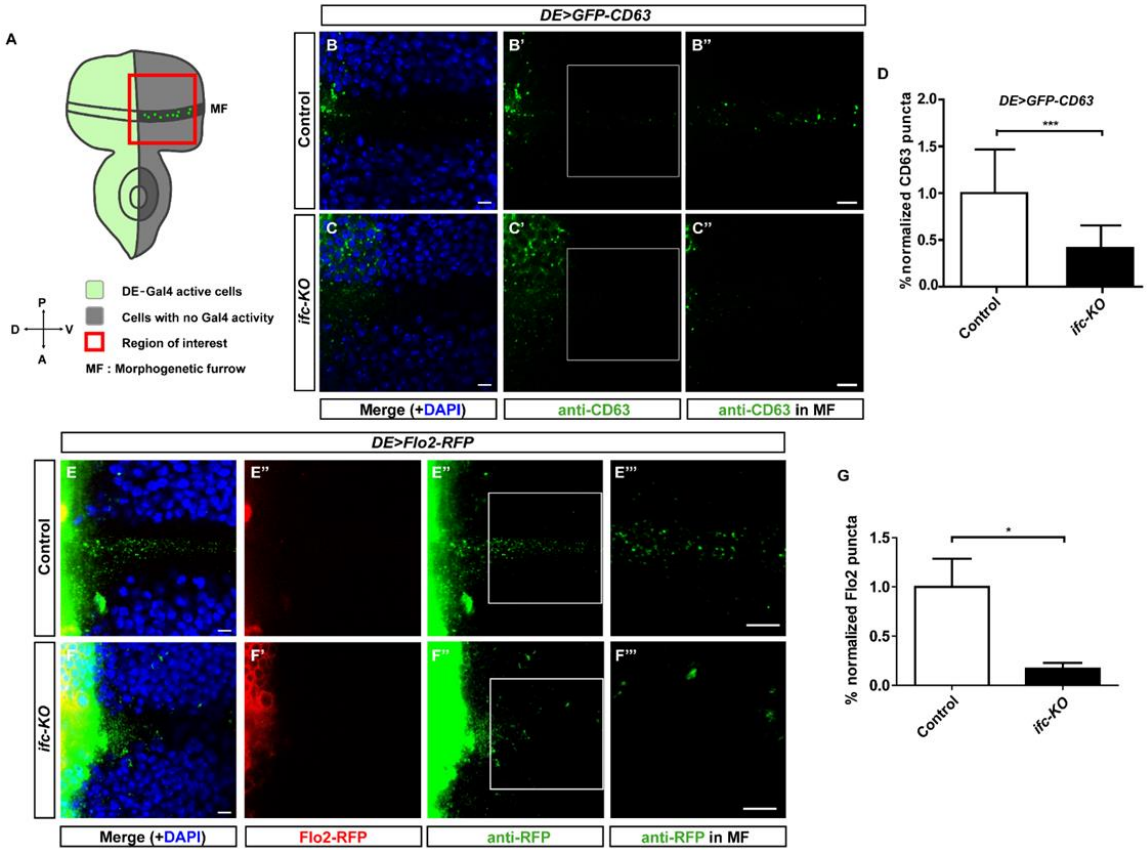

Figure 4. Knocking out *ifc* reduces the number of exosome-like vesicles (ELVs) detected in *Drosophila* eye imaginal discs. (A) A schematic illustration of the *Dorsal-Eye Gal4* (*DE-Gal4*) system for observing the release of ELVs. *DE-Gal4* drives the expression of *UAS-GFP-CD63* in the dorsal half of the eye imaginal disc (mint green). The secreted ELVs that move towards the ventral side alone the morphogenetic furrow (MF) into the area of observation (red box) were counted. **(B-C)** Representative confocal images of *Drosophila* eye imaginal discs with the expression of GFP-CD63 in the dorsal compartment of control (B-B") and *ifc-KO* (C-C") showing signals merged with DAPI in blue (B,C), GFP-CD63 enhanced by anti-CD63 staining in green with the ROIs marked in white boxes (B',C'), and enlarged images of the ROIs with enhanced brightness and contrast to show the GFP-CD63 puncta in the MF (B",C"). **(D)** Quantification of GFP-CD63 puncta. **(E-F)** Representative confocal images of *Drosophila* eye imaginal discs expressing Flo2-RFP in the dorsal compartment in the control (E-E'') and *ifc-KO* eyes (F-F'') showing merged images with DAPI in blue (E,F), Flo2-RFP fluorescence in red (E',F'), Flo2-RPF signal enhanced by anti-RFP staining pseudocolored in green (E",F"), and enlarged and enhanced images of the ROI to reveal Flo2-RFP puncta in the MF in the ROIs (E'''-F'''). **(F)** Quantification of Flo2-RFP puncta. Scale bars: 5 μm. Bar charts show mean ± SEM of at least three independent experiments. *** $p < 0.001$ (Student's *t*-test).

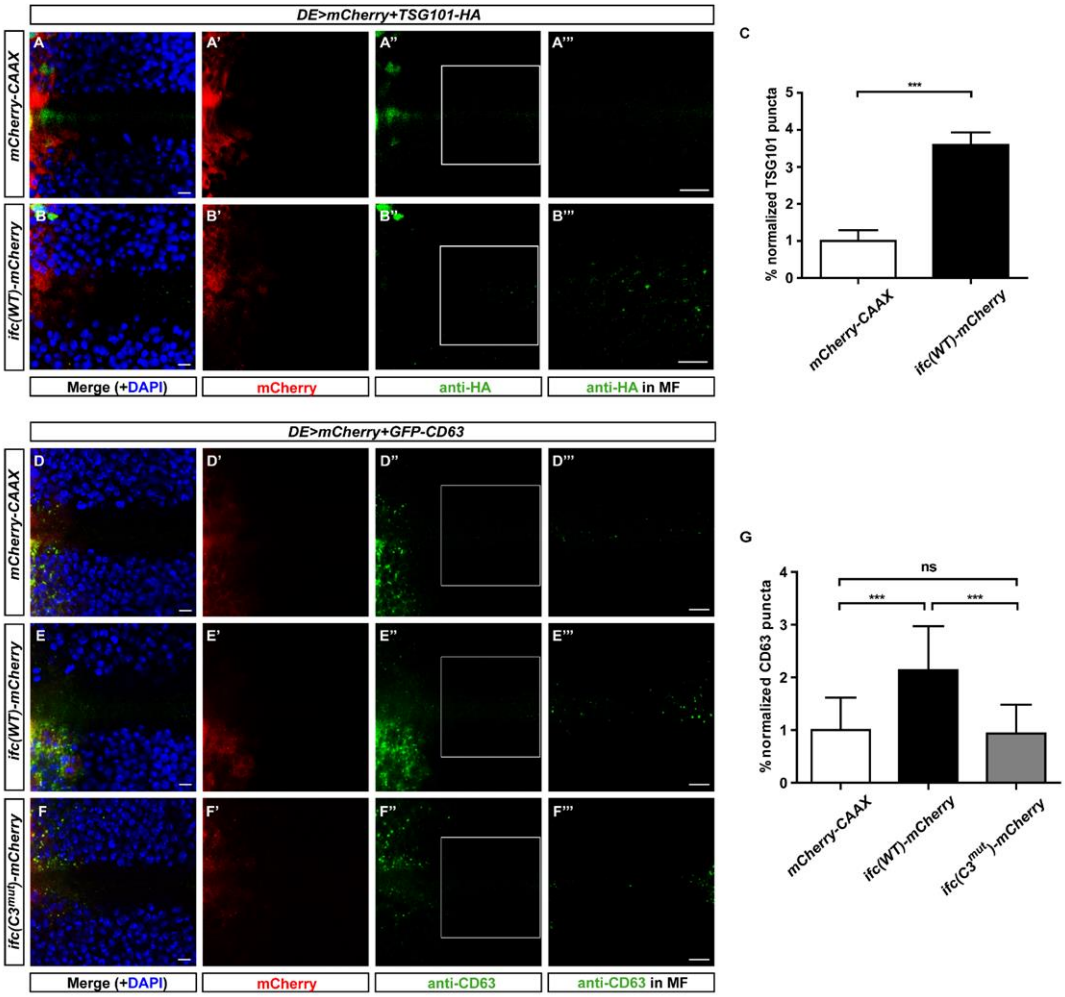

Figure 5. Overexpression of functional Ifc increased the detection of extracellular exosome-like vesicles (ELVs) in *Drosophila* eye imaginal discs. (A-B) Representative confocal images of *Drosophila* eye imaginal discs expressing *TSG101-HA* in the dorsal compartment with *mCherry-CAAX* (control, A-A'''') and *ifc(WT)-mCherry* (B-B'''') showing merged images with DAPI in blue (A,B), mCherry fluorescence in red (A',B'), anti-HA staining in green (A'',B''), and enlarged images of the ROI with enhanced brightness and contrast to reveal TSG101-HA puncta in the MF (A''',B'''). **(C)** Quantification of TSG101-HA puncta. **(D-F)** Representative confocal images of *Drosophila* eye imaginal discs expressing *GFP-CD63* with the control *mCherry-CAAX* (D-D'''), *ifc(WT)-mCherry* (E-E'''), and *ifc(C3^{mut})-mCherry* (F-F''') showing merged images with DAPI in blue (D,E,F), mCherry fluorescence in red (D',E',F'), anti-CD63 staining in green (D'',E'',F''), and enlarged images of the ROI with enhanced brightness and contrast to reveal GFP-CD63 puncta in the MF (D''',E''',F'''). **(G)** Quantification of GFP-CD63 puncta. Scale bars: 5 µm. Bar charts show mean ± SEM of at least three independent experiments. *** $p < 0.001$; ns: Not significant (Student's *t*-test).

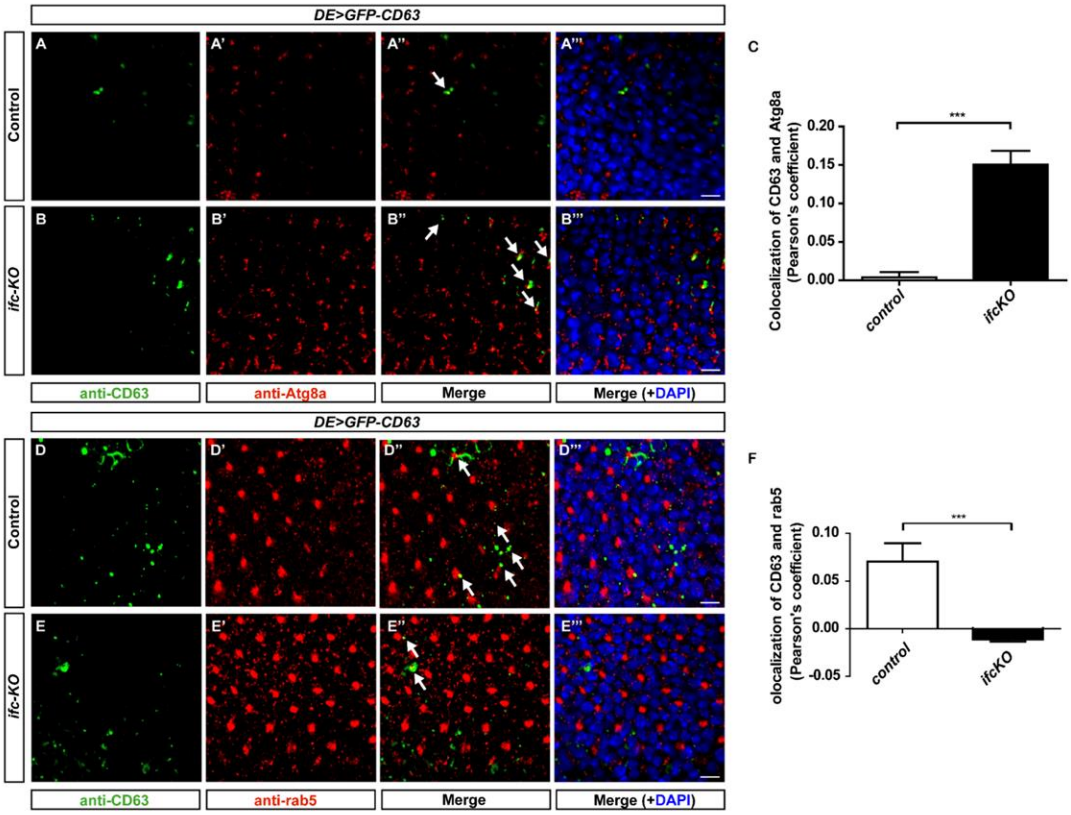

Figure 6. GFP-CD63 becomes more associated with autophagosomes and less with the endosomes in *ifc-KO* eye discs. (A-B) Representative confocal images of *Drosophila* eye imaginal discs expressing *GFP-CD63* in the dorsal compartment in control (A-A'''') and *ifc-KO* (B-B'''') showing anti-CD63 staining in green (A,B), anti-Atg8a staining in red (A',B'), merged images of CD63 and Atg8a immunostaining signals (A'',B''), and merged images with DAPI in blue (A''',B'''). **(C)** Quantification of the colocalization between CD63 and Atg8a. **(D-F)** Representative confocal images of *Drosophila* eye imaginal discs expressing *GFP-CD63* in control (D-D'''') and *ifc-KO* (E-E'''') showing anti-CD63 staining in green (D,E), anti-Rab5 staining in red (D',E'), merged images of CD63 and Rab5 immunostaining signals (D'',E''), and merged images with DAPI in blue (D''',E'''). **(G)** Quantification of the colocalization between CD63 and Rab5. Scale bars: 5 µm. Bar charts show mean ± SEM of at least three independent experiments. *** $p < 0.001$; ns: Not significant (Student's *t*-test).

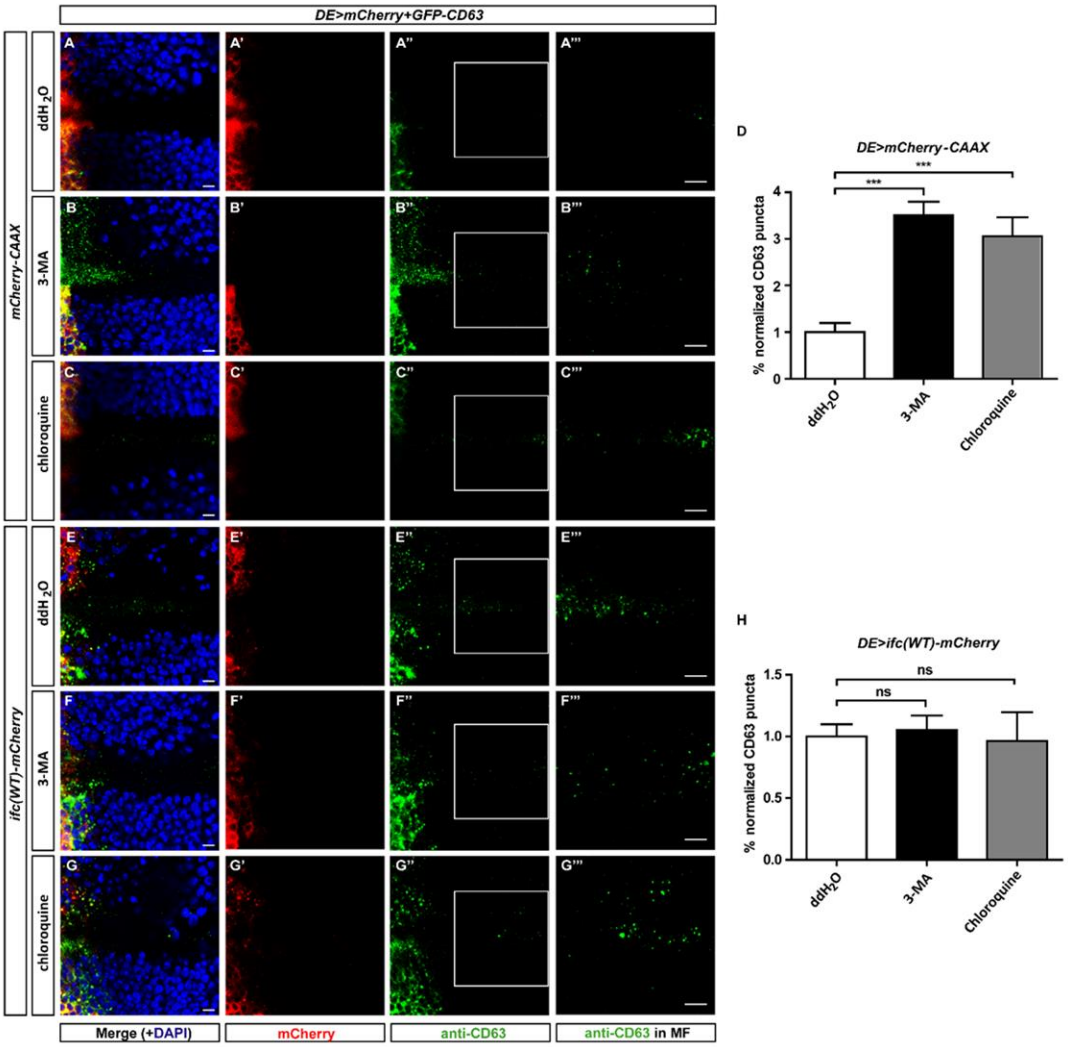

Figure 7. Overexpression of Ifc increases the production of exosome-like vesicles via autophagy inhibition. (A-C) Representative confocal images of *Drosophila* eye imaginal discs expressing *GFP-CD63* in the dorsal compartment treated with ddH_2O solvent (A-A'''), 3-methyladenine (3-MA, B-B'''), and chloroquine (C-C''') showing merged images with DAPI in blue (A,B,C), mCherry control in red (A',B',C'), anti-CD63 staining in green (A'',B'',C''), and enlarged images of the ROI with enhanced brightness and contrast to show GFP-CD63 puncta in the MF (A''',B''',C'''). **(D)** Quantification of GFP-CD63 puncta. **(E-G)** Representative confocal images of *Drosophila* eye imaginal discs expressing GFP-CD63 and *ifc(WT)-mCherry* in the dorsal compartment treated with ddH_2O solvent (E-E'''), 3-methyladenine (3-MA, F-F'''), and chloroquine (G-G''') showing merged images with DAPI in blue (E,F,G), Ifc(WT)-mCherry in red (E',F',G'), anti-CD63 staining in green (E'',F'',G''), and enlarged images of the ROI with enhanced brightness and contrast to show GFP-CD63 puncta in the MF (E''',F''',G'''). **(H)** Quantification of GFP-CD63 puncta. Scale bars: 5 µm. Bar charts show mean ± SEM of at least three independent experiments. *** $p < 0.001$; ns: Not significant (Student's *t*-test).

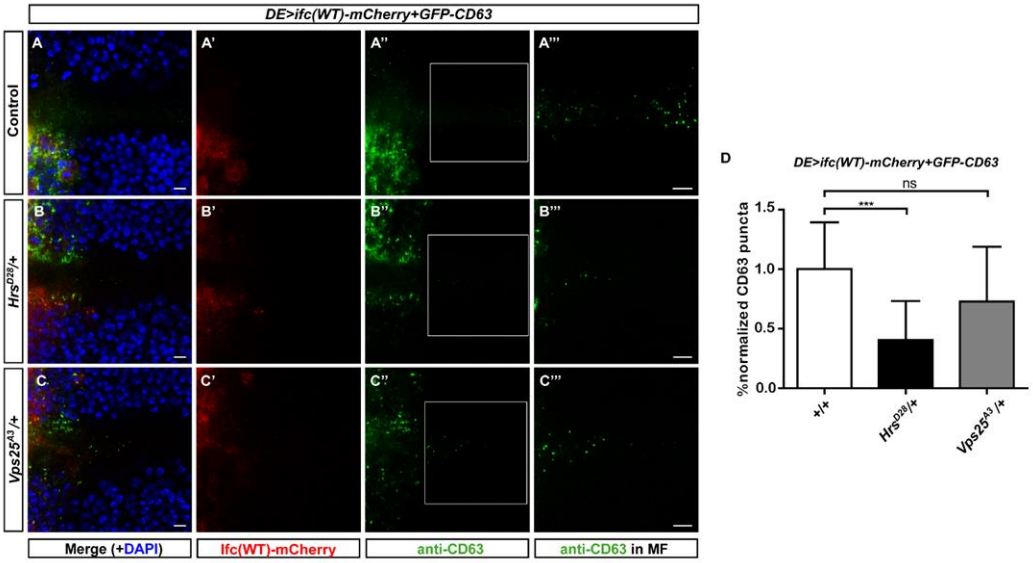

Figure 8. Ifc participates in early exosome biogenesis. (A-C) Confocal images of *Drosophila* eye imaginal discs expressing *GFP-CD63* and *ifc(WT)-mCherry* in the control (A), $Hrs^{D28/+}$ (B), and $Vps25^{A3/+}$ (C) showing merged images with DAPI in blue (A,B,C), mCherry fluorescence in red (A',B',C'), anti-CD63 staining in green (A",B",C"), and enlarged images of the ROI with enhanced brightness and contrast to reveal GFP-CD63 puncta in the MF in the ROIs (A'",B'",C'"). **(D)** Quantification of GFP-CD63 puncta. Scale bars: 5 µm. Bar charts show mean ± SEM of at least three independent experiments. *** $p < 0.001$, ns: Not significant (one-way ANOVA).

A

dhCer	DEGS1	ILV (%)	N
-	-	0%	10
-	+	0%	10
dhCer	-	0%	20
dhCer	+	31.81%	22

F

DEGS1	Fenretinide	ILV (%)	N
-	EtOH	0%	10
+	EtOH	36.36%	11
-	+	0%	9
+	+	0%	9

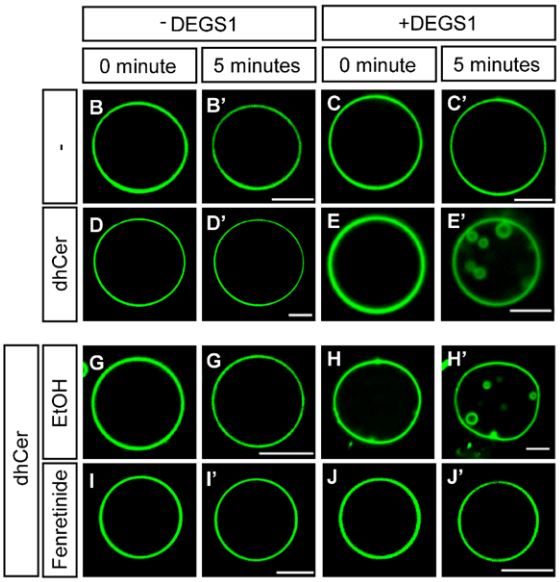

Figure 9. DEGS1 promotes the formation of ILVs in the giant unilamellar vesicles (GUVs) *in vitro*. **(A)** The percentages of GUVs that formed ILVs within 5 min. The GUVs were composed of DOPC:cholesterol at the molar ratio of 1:0.67 with or without dhCer and recombinant DEGS1 protein. **(B-E)** Representative images of GUVs in (A). **(F)** The percentages of GUVs that showed ILV formation within 5 min. The GUVs consisted of DOPC:cholesterol:dhCer at the molar ratio of 1:1:0.67 with and without DEGS1 protein in the presence of ethanol (EtOH) solvent or 0.2 μM fenretinide, a DEGS1 inhibitor. **(G-J)** Representative images of GUVs in (F). Scale bar: 5 μm.